A Reversible and Higher-Rate Li-O_2 Battery

Zhangquan Peng *et al.*

Science **337**, 563 (2012);
DOI: 10.1126/science.1223985

A Reversible and Higher-Rate Li-O_2 Battery

Zhangquan Peng, Stefan A. Freunberger,* Yuhui Chen, Peter G. Bruce†

The rechargeable nonaqueous lithium-air (Li-O_2) battery is receiving a great deal of interest because, theoretically, its specific energy far exceeds the best that can be achieved with lithium-ion cells. Operation of the rechargeable Li-O_2 battery depends critically on repeated and highly reversible formation/decomposition of lithium peroxide (Li_2O_2) at the cathode upon cycling. Here, we show that this process is possible with the use of a dimethyl sulfoxide electrolyte and a porous gold electrode (95% capacity retention from cycles 1 to 100), whereas previously only partial Li_2O_2 formation/decomposition and limited cycling could occur. Furthermore, we present data indicating that the kinetics of Li_2O_2 oxidation on charge is approximately 10 times faster than on carbon electrodes.

A typical rechargeable nonaqueous Li-O_2 cell is composed of a Li metal anode (negative electrode), a nonaqueous Li^+ conducting electrolyte, and a porous cathode (positive electrode) (*1*–*6*). Operation of the cell depends critically on O_2 being reduced at the cathode to O_2^{2-}, which combines with Li^+ from the electrolyte to form Li_2O_2 on discharge, and the reverse reaction occurring during charging (*1*–*6*). Early investigation of nonaqueous Li-O_2 cells focused on the use of organic carbonate–based electrolytes, which have since been shown to decompose irreversibly at the cathode on discharge to form products such as lithium formate (HCO_2Li), lithium acetate (CH_3CO_2Li), lithium propyl-dicarbonate [$C_3H_6(CO_2Li)_2$], and lithium carbonate (Li_2CO_3) with little or no evidence of Li_2O_2 formation (*7*–*11*). Later work turned to ethers—while initially promising and certainly more stable to reduced O_2 species than organic carbonates, ethers exhibit increasing electrolyte decomposition upon cycling (figs. S1 to S3) (*11*–*13*). These data show that whether combined with carbon or nanoporous gold (NPG) electrodes, ethers, including dimethoxyethane (DME), are increasingly unstable upon cycling. For example, in the case of DME-based electrolytes after only 10 cycles, 20% of the discharge products arise from electrolyte decomposition (fig. S2). Such side reactions can be difficult to detect by x-ray diffraction because of poor crystallinity of the decomposition products. Similar decomposition of tetraethylene glycol dimethyl ether (tetraglyme)–based electrolytes has been reported (*12*) and is also shown to occur at a NPG electrode (fig. S3). These results demonstrate that ethers do not support the necessary reversible Li_2O_2 formation/decomposition upon cycling that is essential for operation of the Li-O_2 cell. A very recent paper comes to a different conclusion from the papers cited above and from our own results concerning the cyclability of the tetraglyme/carbon interface (*14*).

We constructed a Li-O_2 cell that contained an electrolyte composed of 0.1 M $LiClO_4$ in dimethyl sulfoxide (DMSO) and a NPG cathode [for details, see the supplementary materials and methods section (*15*)]. The cell was operated in 1 atm of O_2. Oxygen reduction electrochemistry at the DMSO/planar-carbon interface has been studied previously (*16*). Discharge/charge curves for the cell on cycles 1, 5, 10, and 100 are shown in Fig. 1. Most of the initial capacity (95%) is retained after 100 cycles. However, as is now recognized from the work of many authors, the ability to recharge a Li-O_2 cell is not proof that the reactions occurring at the positive electrode are reversible and involve Li_2O_2 formation/decomposition (*7*–*13*). To demonstrate that the reaction at the porous cathode is Li_2O_2 formation/decomposition, we collected Fourier transform infrared (FTIR) spectroscopy data at the end of discharge and charge as a function of cycle number (1, 5, 10, and 100) (Fig. 2A). At the end of each discharge, we observed Li_2O_2. Its formation was corroborated by in situ surface-enhanced Raman spectroscopy (SERS) carried out on a cell with a sapphire window for transmission of the Raman laser beam (Fig. 2B) (*17*). A few small peaks, in addition to the peaks arising from Li_2O_2, are apparent in the

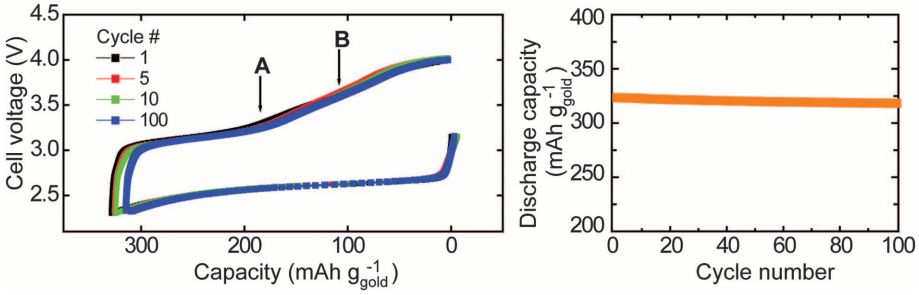

Fig. 1. Charge/discharge curves (**left**) and cycling profile (**right**) for a Li-O_2 cell with a 0.1 M $LiClO_4$-DMSO electrolyte and a NPG cathode, at a current density of 500 mAg^{-1} (based on the mass of Au). Because the capacities are given per gram of Au, which is ~10-fold heavier (more dense) than carbon, 300 $mAhg^{-1}$ (based on the mass of Au) would, for the same porous electrode but formed from carbon, correspond to ~3000 $mAhg^{-1}$ (based on the mass of carbon). FTIR spectra collected upon charging at points A and B are shown in fig. S7.

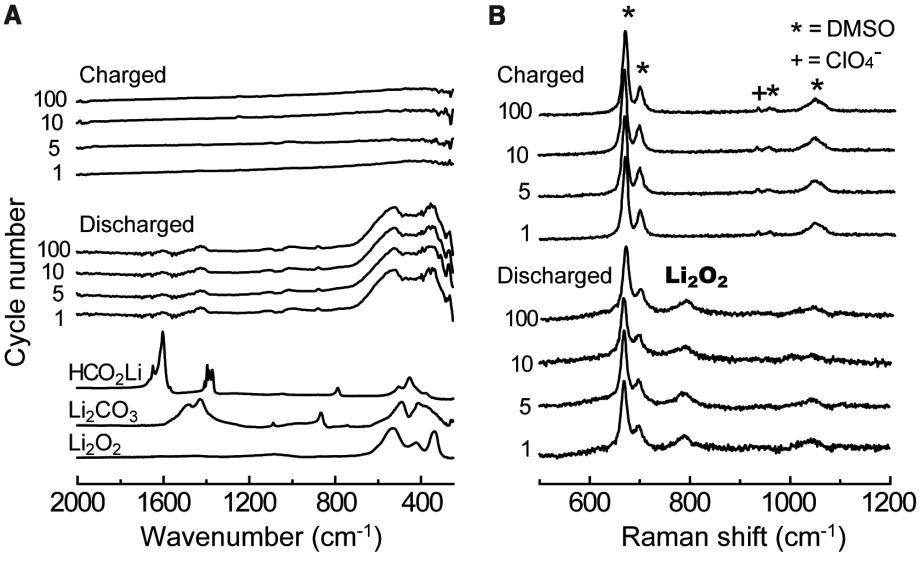

Fig. 2. Vibrational spectra of a NPG cathode at the end of discharge and charge in 0.1 M $LiClO_4$-DMSO. (**A**) FTIR and (**B**) SERS spectra.

School of Chemistry, University of St. Andrews, North Haugh, St. Andrews, Fife KY16 9ST, UK.

*Present address: Institute for Chemistry and Technology of Materials, Graz University of Technology, Stremayrgasse 9, 8010 Graz, Austria.

†To whom correspondence should be addressed. E-mail: p.g.bruce@st-andrews.ac.uk

FTIR spectra at the end of discharge, at ~880, 1420, 1490, and 1600 cm^{-1}. These peaks could be assigned to a mixture of Li_2CO_3 and HCO_2Li, with no other species being detected, such as from S containing decomposition products (Fig. 2A). The presence of HCO_2Li was confirmed by washing the NPG electrode at the end of discharge with D_2O and examining the resulting solution by ^1H nuclear magnetic resonance (NMR), following the procedure described previously (*7*, *12*). HCO_2D in the ^1H NMR indicated the presence of HCO_2Li in the discharged electrode before washing.

Batteries and chemical/electrochemical reactions in general exhibit some degree of side reaction, particularly on the first cycle (e.g., Li-ion batteries). The key question is the extent of such side reactions: whether this is sufficiently small compared with the amount of electrolyte used in practical cells and whether the extent increases with cycling. We prepared mechanical mixtures of Li_2O_2 with Li_2CO_3 and Li_2O_2 with HCO_2Li of varying ratios, collected their FTIR spectra, and constructed calibration curves (figs. S4 and S5); from these curves, we determined the fractions of Li_2CO_3 and HCO_2Li in the FTIR spectra in Fig. 2 to be <1%. The proportion of Li_2O_2 at the end of discharge exceeds 99%, and there is no evidence of this proportion decreasing on cycling. We used ^1H and ^{13}C NMR to investigate the presence of any solution-soluble decomposition products. Sensitivity to detection of such species depends on the ratio between the amount of electrolyte and the amount of discharge product (*15*). We collected spectra after 100 cycles to concentrate any decomposition products, but we did not detect evidence of any such species (fig. S6). We used differential electrochemical mass spectrometry (DEMS) to obtain further confirmation that discharge was overwhelmingly dominated by Li_2O_2 formation. The DEMS process involves in situ mass spectrometric analysis of the gases consumed/evolved during a slow-sweep (0.1 mVs^{-1}) linear potential scan (Fig. 3A) (*15*). The only gas detected on discharge was O_2. There was no evidence of CO_2, SO_2, or SO_3 (i.e., no evidence of electrolyte decomposition), in contrast to other electrolytes. The high purity of Li_2O_2 formation implies that for every two electrons (e^-) passed, one O_2 molecule should be consumed; that is, the charge-to-mass ratio should be $2e^-/O_2$. The O_2 consumption on discharge follows the cell current (Fig. 3A), and the charge-to-mass ratio is $2e^-/O_2$ on each discharge (Table 1).

The FTIR spectra collected at the end of charge on cycles 1, 5, 10, and 100 are shown in Fig. 2A, from which it is clear that the product formed on discharge has been removed upon charging. This observation was confirmed by the SERS data in Fig. 2B, where the characteristic peak for Li_2O_2 at ~800 cm^{-1}, observed at the end of discharge, is absent from the spectrum at the end of charge. To probe the oxidation in more detail, we used DEMS on charging for cycles 1, 5, 10, and 100 (Fig. 3B). Only O_2 was

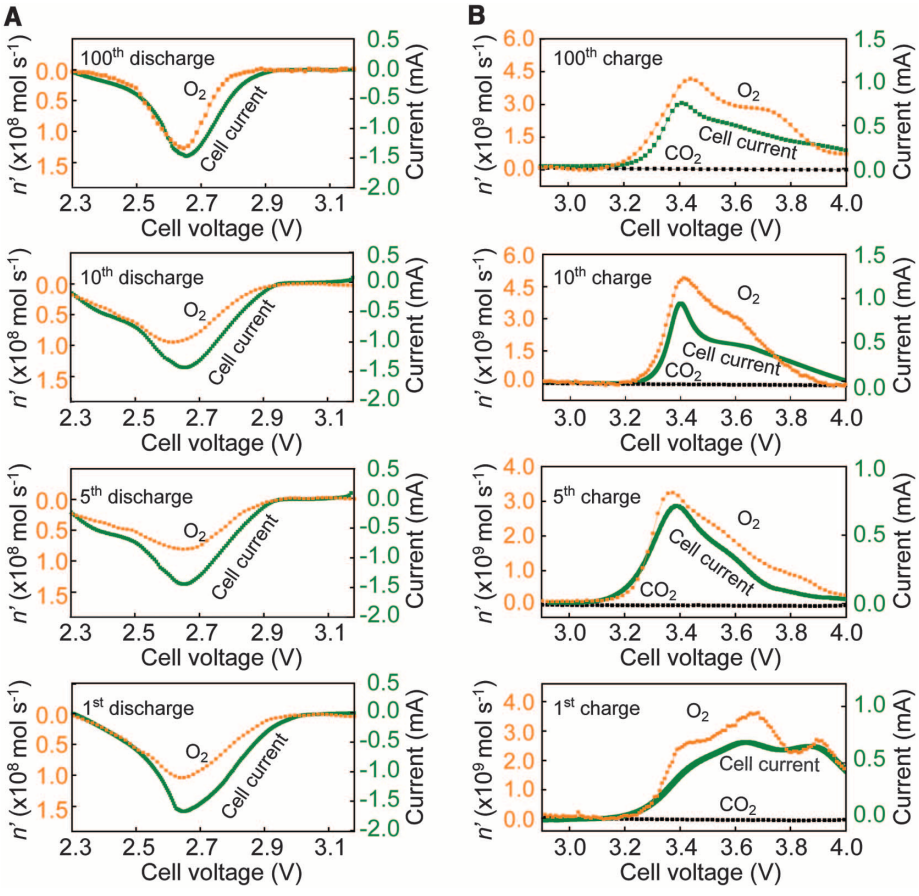

Fig. 3. DEMS of a NPG cathode during (**A**) discharge and (**B**) charge in 0.1 M $LiClO_4$-DMSO. Linear potential scans at 0.1 mVs^{-1} (corresponding to a low rate of discharge/charge) between 2.3 and 4.0 V were used. *n'* indicates the gas-consumption/-generation rates during discharge and charge.

detected, confirming that Li_2O_2 had formed on the previous discharge and also that the electrolyte, even in the presence of Li_2O_2, is stable on oxidation. Upon examining the linear voltammetry (current-voltage curve) in Fig. 3B, several peaks are evident, corresponding well with the peaks for O_2 evolution. A similar heterogeneous oxidation process spanning a range of potentials has been observed previously in porous electrodes and has been ascribed to oxidation of Li_2O_2 being easier in certain pores than in others (*11*). We collected FTIR spectra (fig. S7) during charging, at the points shown in Fig. 1. The spectra indicate that the quantity of Li_2O_2 is diminishing with increasing state of charge, but that some Li_2O_2 is still present at point B. The ratio of charge passed to O_2 evolved on charging is given in Table 1. As was the case for discharge, the ratio is close to $2e^-/O_2$ on each cycle, in accord with charging involving oxidation of Li_2O_2 without electrolyte degradation. Over the collection of up to 100 cycles, the results from FTIR, SERS, NMR, and DEMS all demonstrate that the cell cycles by the reversible formation/decomposition of Li_2O_2.

To investigate whether the dominance of Li_2O_2 formation/decomposition is due to the salt,

Table 1. Ratios of the number of electrons to oxygen molecules upon reduction (discharge) and oxidation (charge).

Cycle number	Discharge e^-/O_2	Charge e^-/O_2
1	2.01	1.98
5	1.99	2.04
10	2.02	1.98
100	2.03	2.01

solvent, or electrode substrate, we constructed cells in which $LiClO_4$ was replaced by LiTFSI [lithium bis(trifluoromethanesulfonyl)imide] and separately in which the NPG electrode was replaced by carbon black (Super P, Timcal, Bodio, Switzerland). In the former case, the load curves and FTIR spectra at the end of discharge and charge on cycling are the same as those for $LiClO_4$ (fig. S8), demonstrating that changing the salt does not influence the results. In contrast, replacing the NPG electrode with carbon does adversely affect the results (Fig. 4). The FTIR at the end of discharge on carbon shows a greater proportion of side reaction, Li_2CO_3, and HCO_2Li (Fig. 4). Using calibration plots, as before, we estimate the total

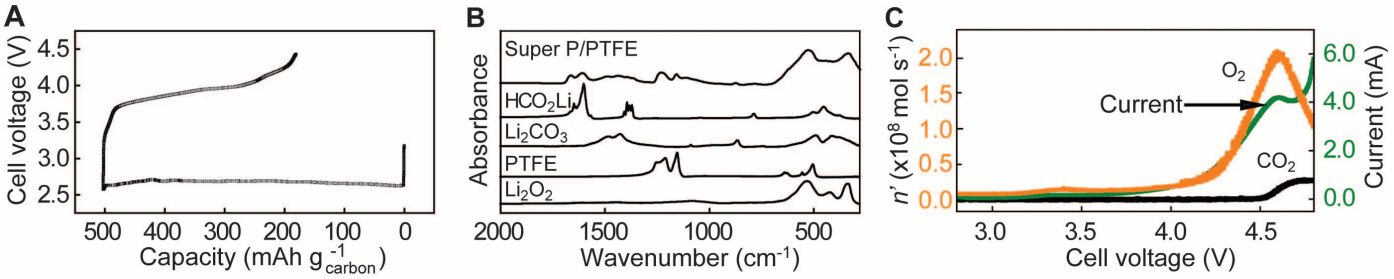

Fig. 4. (**A**) Discharge-charge curve of a Li-O_2 cell employing a composite carbon cathode at 70 mAg^{-1} (normalized to the mass of carbon). (**B**) FTIR at the end of discharge. (**C**) DEMS of the porous carbon cathode during charging in 0.1 M $LiClO_4$-DMSO; scan rate 0.1 mVs^{-1}. The composition of the cathode is Super P carbon:polytetrafluoroethylene (PTFE) 8:2 (m/m). *n'* indicates the gas-generation rates during the charging process.

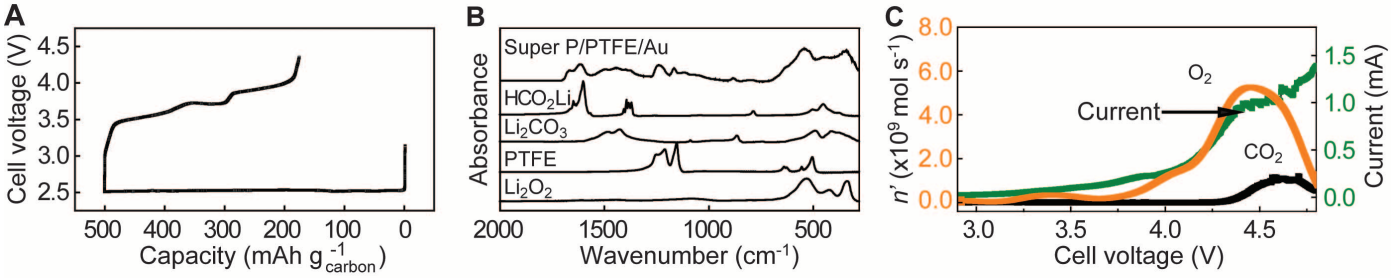

Fig. 5. (**A**) Discharge-charge curve of a Li-O_2 cell employing a gold-loaded composite carbon cathode at 70 mAg^{-1} (normalized to the mass of carbon). (**B**) FTIR at the end of discharge. (**C**) DEMS of gold-loaded porous carbon cathode [Super P:PTFE:Au 8:1:1 (m/m)] during charging in 0.1 M $LiClO_4$-DMSO; scan rate 0.1 mVs^{-1}. *n'* indicates the gas-generation rates during the charging process. Note the electrode area is ¼ of that in Fig. 4.

proportion of side-reaction products to be ~15%. The carbon itself may be unstable, as suggested recently (*18*), although the HCO_2Li formation is likely to involve DMSO. Further work is required to investigate the origin of the side products formed at the DMSO/carbon interface. The charging curve (Fig. 4) is also different from the NPG electrode (Fig. 1). The voltage rises rapidly, passes through a very small step at 3.3 V to ~3.75 V, then slowly to 4 V. The higher charging voltage for carbon versus NPG occurs despite the current density (based on the true surface area of the electrode) being less for the carbon electrode than for NPG: 0.1 μAcm^{-2} (true surface area of carbon) compared with 1 μAcm^{-2} (true surface area of NPG). Note that the kinetics of the different electrodes is discussed below. The DEMS data in Fig. 4 confirm a very minor degree of O_2 evolution at 3.3 to 3.4 V, with most of the O_2 being evolved above 4 V and a substantial amount above 4.5 V, where it is accompanied by CO_2 evolution, which is indicative of electrolyte oxidation. The DEMS data for the Super P carbon cathode in Fig. 4 contrast strongly with those for the NPG electrode in Fig. 3B, where O_2 evolution commences at ~3.2 V and all of the O_2 is evolved below 4 V (Table 1 confirms that all of the O_2 expected from the Li_2O_2 present is evolved). These results indicate that NPG lowers the charging voltage (i.e., NPG is more effective than carbon at promoting Li_2O_2 oxidation).

The DEMS results for the Super P cathode are in accord with the difficulty in cycling a cell with a carbon electrode. Incorporation of α-MnO_2 nanowires into a porous carbon electrode proved effective in promoting Li_2O_2 oxidation in previous studies (*19*). However, reduction of O_2 in the DMSO electrolyte at a Super P electrode incorporating α-MnO_2 nanowires resulted in the formation of LiOH on the first discharge, as noted in previous studies in ethers, possibly arising from –OH groups on the surface of the oxide (*12*). Therefore, we constructed a composite electrode made of Super P with nanoparticulate gold (*15*). The results are shown in Fig. 5. As for Super P alone, the side products are Li_2CO_3 and HCO_2Li, which together account for ~15% of the discharge products. Charging occurs at a somewhat lower voltage than without the Au, as noted previously (*20*), but overall nanoparticulate Au/carbon composite electrodes are less effective at promoting Li_2O_2 oxidation than NPG electrodes. This is especially evident when comparing the DEMS data in Figs. 3, 4, and 5: Whereas only a small proportion of O_2 is evolved at the carbon electrode below 4 V (Fig. 4), the proportion increases somewhat with the addition of nanoparticulate Au to the electrode (Fig. 5), but it is much greater for NPG (Fig. 3).

An important challenge for Li-O_2 cells is to increase the kinetics of the electrode reaction, which is generally observed to be relatively low, especially for the charging process (*1*–*6*, *21*–*33*). The rate used in Fig. 1 is 500 mAg^{-1} of gold (equivalent to ~5000 mAg^{-1} for a carbon electrode of the same volume), which translates into 1.0 μAcm^{-2} based on the total active surface area of the NPG electrode (50 m^2g^{-1}) (*15*). The rate used for the carbon-based electrodes (Figs. 4 and 5) is 70 mAg^{-1}, a typical value from the literature (*19*, *24*), which translates into a true current density of 0.1 μAcm^{-2}, based on a surface area for Super P of ~60 m^2g^{-1}. Therefore, the true rate at the electrode surface is 10 times greater in the case of NPG than is typical for carbon electrodes. Yet, this is still a relatively low rate overall. The discharge potential is hardly affected by the change in rate, but as noted above, a substantial proportion of the charging occurs at lower voltages for NPG than for carbon or Super P/nanoparticulate Au, despite the rate being 10-fold higher for NPG. This result underlines the fact that oxidation of Li_2O_2 on NPG is much more facile than on carbon. Other factors, such as electrode porosity, can also affect rate performance, and this will differ between NPG and Super P. Recent studies of the electrocatalysis of O_2 evolution on charging Li_2O_2 suggest that there is little evidence of true electrocatalysis (*24*). We do not claim electrocatalysis is necessarily taking place here, but we simply observe that the charging voltage is lower and kinetics is faster compared with a carbon electrode. Although the capacity obtained with NPG in Fig. 1 may look relatively modest at ~300 $mAhg^{-1}$, it must be noted that this value is normalized to the mass of gold and is equivalent to 3000 $mAhg^{-1}$ of carbon.

In conclusion, we have shown that a Li-O_2 cell composed of a DMSO-based electrolyte and a NPG electrode can sustain reversible cycling, retaining 95% of its capacity after 100 cycles and having >99% purity of Li_2O_2 formation at the cathode, even on the 100th cycle, and its complete oxidation on charge. The charge-to-

mass ratio on discharge and charge is $2e^-/O_2$, confirming that the reaction is overwhelmingly Li_2O_2 formation/decomposition. We have also shown that such electrodes are particularly effective at promoting the decomposition of Li_2O_2, with all the Li_2O_2 being decomposed below 4 V and ~50% decomposed below 3.3 V, at a rate approximately one order of magnitude higher than on carbon. Although DMSO is not stable with bare Li anodes, it could be used with protected Li anodes. Nanoporous Au electrodes are not suitable for practical cells, but if the same benefits could be obtained with Au-coated carbon, then low-mass electrodes would be obtained, although cost may still be a problem. A cathode reaction overwhelmingly dominated by Li_2O_2 formation on discharge, its complete oxidation on charge and sustainable on cycling, is an essential prerequisite for a rechargeable nonaqueous Li-O_2 battery. Hence, the results presented here encourage further study of the rechargeable nonaqueous Li-O_2 cell, although many challenges to practical devices remain.

References and Notes

1. K. M. Abraham, Z. Jiang, *J. Electrochem. Soc.* **143**, 1 (1996).
2. P. G. Bruce, S. A. Freunberger, L. J. Hardwick, J.-M. Tarascon, *Nat. Mater.* **11**, 19 (2012).
3. G. Girishkumar, B. McCloskey, A. C. Luntz, S. Swanson, W. Wilcke, *J. Phys. Chem. Lett.* **1**, 2193 (2010).
4. B. Scrosati, J. Hassoun, Y.-K. Sun, *Energy Environ. Sci.* **4**, 3287 (2011).
5. J.-G. Zhang, P. G. Bruce, X. G. Zhang, in *Handbook of Battery Materials*, C. Daniel, J. O. Besenhard, Eds. (Wiley-VCH, Weinheim, Germany, ed. 2, 2011), pp. 759–811.
6. J. Christensen *et al.*, *J. Electrochem. Soc.* **159**, R1 (2012).
7. S. A. Freunberger *et al.*, *J. Am. Chem. Soc.* **133**, 8040 (2011).
8. F. Mizuno, S. Nakanishi, Y. Kotani, S. Yokoishi, H. Iba, *Electrochemistry* **78**, 403 (2010).
9. W. Xu *et al.*, *J. Power Sources* **196**, 3894 (2011).
10. G. M. Veith, N. J. Dudney, J. Howe, J. Nanda, *J. Phys. Chem. C* **115**, 14325 (2011).
11. B. D. McCloskey, D. S. Bethune, R. M. Shelby, G. Girishkumar, A. C. Luntz, *J. Phys. Chem. Lett.* **2**, 1161 (2011).
12. S. A. Freunberger *et al.*, *Angew. Chem. Int. Ed.* **50**, 8609 (2011).
13. H. Wang, K. Xie, *Electrochim. Acta* **64**, 29 (2012).
14. H.-G. Jung, J. Hassoun, J.-B. Park, Y.-K. Sun, B. Scrosati, *Nat. Chem.* **4**, 579 (2012).
15. Materials and methods are available as supplementary materials on *Science* Online.
16. C. O. Laoire, S. Mukerjee, K. M. Abraham, E. J. Plichta, M. A. Hendrickson, *J. Phys. Chem. C* **114**, 9178 (2010).
17. Z. Peng *et al.*, *Angew. Chem. Int. Ed.* **50**, 6351 (2011).
18. B. D. McCloskey *et al.*, *J. Phys. Chem. Lett.* **3**, 997 (2012).
19. A. Débart, A. J. Paterson, J. Bao, P. G. Bruce, *Angew. Chem. Int. Ed.* **47**, 4521 (2008).
20. C. J. Allen, S. Mukerjee, E. J. Plichta, M. A. Hendrickson, K. M. Abraham, *J. Phys. Chem. Lett.* **2**, 2420 (2011).
21. Y.-C. Lu *et al.*, *Energy Environ. Sci.* **4**, 2999 (2011).
22. Y.-C. Lu, H. A. Gasteiger, Y. Shao-Horn, *J. Am. Chem. Soc.* **133**, 19048 (2011).
23. T. Ogasawara, A. Débart, M. Holzapfel, P. Novák, P. G. Bruce, *J. Am. Chem. Soc.* **128**, 1390 (2006).
24. B. D. McCloskey *et al.*, *J. Am. Chem. Soc.* **133**, 18038 (2011).
25. S. J. Visco, B. D. Katz, Y. S. Nimon, L. D. DeJonghe, U.S. Patent 7,282,295 (2007).
26. X.-H. Yang, P. He, Y.-Y. Xia, *Electrochem. Commun.* **11**, 1127 (2009).
27. J. Read, *J. Electrochem. Soc.* **149**, A1190 (2002).
28. Y. G. Wang, H. S. Zhou, *J. Power Sources* **195**, 358 (2010).
29. J. S. Hummelshøj *et al.*, *J. Chem. Phys.* **132**, 071101 (2010).
30. V. S. Bryantsev, M. Blanco, F. Faglioni, *J. Phys. Chem. A* **114**, 8165 (2010).
31. Y. Mo, S. P. Ong, G. Ceder, *Phys. Rev. B* **84**, 205446 (2011).
32. D. Aurbach, M. Daroux, P. Faguy, E. Yeager, *J. Electroanal. Chem.* **297**, 225 (1991).
33. J. Hassoun, F. Croce, M. Armand, B. Scrosati, *Angew. Chem. Int. Ed.* **50**, 2999 (2011).

Acknowledgments: P.G.B. is indebted to the UK Engineering and Physical Sciences Research Council, including the Supergen Programme and Alistore for financial support.

Supplementary Materials

www.sciencemag.org/cgi/content/full/science.1223985/DC1
Materials and Methods
Figs. S1 to S9
References (*34*, *35*)

30 April 2012; accepted 26 June 2012
Published online 19 July 2012;
10.1126/science.1223985

Aerosols from Overseas Rival Domestic Emissions over North America

Hongbin Yu,[1,2]* Lorraine A. Remer,[3] Mian Chin,[2] Huisheng Bian,[2,3] Qian Tan,[2,4] Tianle Yuan,[2,3] Yan Zhang[2,4]

Many types of aerosols have lifetimes long enough for their transcontinental transport, making them potentially important contributors to air quality and climate change in remote locations. We estimate that the mass of aerosols arriving at North American shores from overseas is comparable with the total mass of particulates emitted domestically. Curbing domestic emissions of particulates and precursor gases, therefore, is not sufficient to mitigate aerosol impacts in North America. The imported contribution is dominated by dust leaving Asia, not by combustion-generated particles. Thus, even a reduction of industrial emissions of the emerging economies of Asia could be overwhelmed by an increase of dust emissions due to changes in meteorological conditions and potential desertification.

Atmospheric aerosols emitted or produced in one region can be transported thousands of miles downwind to affect other regions on intercontinental or hemispheric scales (*1*–*3*). Because of such intercontinental transport, emission controls over North America may be offset partly by the import of aerosols from remote international sources. Assessing the aerosol intercontinental transport and its impacts on atmospheric composition, air quality, and climate in North America is thus needed from both scientific and policy perspectives. Currently, such assessment for the most part has been based on global model simulations (*4*–*6*) and remains very uncertain (*7*).

Today's constellation of passive and active satellite sensors are providing three-dimensional distributions of aerosol properties on a global scale, with improved accuracy for aerosol optical depth (AOD) and enhanced capability of characterizing aerosol type (*8*). Such advances have made it feasible to elucidate the evolution of aerosol plumes during the cross-ocean transport (*9*, *10*) and generate measurement-based estimates of aerosol intercontinental transport on seasonal and annual time scales (*11*, *12*).

We integrated satellite measurements from the Moderate-resolution Imaging Spectroradiometer (MODIS) (*13*) and the Cloud-Aerosol Lidar with Orthogonal Polarization (CALIOP) (*14*) in order to characterize the three-dimensional distributions of trans-Pacific dust transport (*15*). We used MODIS measurements of total AOD and fine-mode fraction over ocean to separate AOD for dust, combustion aerosol, and marine aerosol (*16*). Combustion aerosol refers to aerosol products from the burning of both biomass and fossil fuels, which include sulfates, nitrates, and carbonaceous particles. The partitioning of AOD into these three categories accounts for fine-mode components of marine and dust aerosol (*15*, *16*). The CALIOP measurements are used to characterize seasonal variations of aerosol extinction profiles, with dust being separated from other types of aerosols by the measured depolarization ratio (*15*). The climatology of springtime (March-April-May, or MAM) AOD (2001–2007) and vertical profile of extinction (2006–2010) over the North Pacific basin are shown in Fig. 1. Spring is the most active season for trans-Pacific transport of combustion aerosols and dust because of the combined effect of active extratropical cyclones and the strongest mid-latitude westerlies. However, trans-Pacific transport occurs throughout the year (*12*). Over the period we examined here, interannual variations of AOD are generally small for dust in the outflow and inflow regions (8 and 4%, respectively), but larger (17 and 18%, respectively) for combustion aerosol. The relatively large interannual variations for combustion

[1]Earth System Science Interdisciplinary Center, University of Maryland, College Park, MD 20740, USA. [2]Earth Science Directorate, NASA Goddard Space Flight Center, Greenbelt, MD 20771, USA. [3]Joint Center for Earth Systems Technology, University of Maryland at Baltimore County, Baltimore, MD 21228, USA. [4]Goddard Earth Sciences Technology and Research Center, Universities Space Research Association, Columbia, MD 21044, USA.

*To whom correspondence should be addressed. E-mail: hongbin.yu@nasa.gov